The Astrophysical Journal Letters, 968:L7 (8pp), 2024 June 10 https://doi.org/10.3847/2041-8213/ad4edb

NICER Discovery that SRGA J144459.2–604207 Is an Accreting Millisecond X-Ray Pulsar

Mason Ng[1], Paul S. Ray[2], Andrea Sanna[3], Tod E. Strohmayer[4,5], Alessandro Papitto[6], Giulia Illiano[6,7,8], Arianna C. Albayati[9], Diego Altamirano[9], Tuğba Boztepe[10], Tolga Güver[11,12], Deepto Chakrabarty[1], Zaven Arzoumanian[4], D. J. K. Buisson[13], Elizabeth C. Ferrara[4,14,15], Keith C. Gendreau[4], Sebastien Guillot[16,17], Jeremy Hare[4,15,18], Gaurava K. Jaisawal[19], Christian Malacaria[20], and Michael T. Wolff[2]
[1] MIT Kavli Institute for Astrophysics and Space Research, Massachusetts Institute of Technology, Cambridge, MA 02139, USA; masonng@mit.edu
[2] Space Science Division, U.S. Naval Research Laboratory, Washington, DC 20375, USA
[3] Dipartimento di Fisica, Università degli Studi di Cagliari, SP Monserrato-Sestu km 0.7, I-09042 Monserrato, Italy
[4] Astrophysics Science Division, NASA Goddard Space Flight Center, Greenbelt, MD 20771, USA
[5] Joint Space-Science Institute, NASA Goddard Space Flight Center, Greenbelt, MD 20771, USA
[6] INAF-Osservatorio Astronomico di Roma, Via Frascati 33, I-00040 Monte Porzio Catone (RM), Italy
[7] Dipartimento di Fisica, Università degli Studi di Roma "Tor Vergata," Via della Ricerca Scientifica 1, I-00133 Roma, Italy
[8] Dipartimento di Fisica, Università degli Studi di Roma "La Sapienza," Piazzale Aldo Moro 5, I-00185 Roma, Italy
[9] School of Physics and Astronomy, University of Southampton, Southampton SO17 1BJ, UK
[10] Istanbul University, Graduate School of Sciences, Department of Astronomy and Space Sciences, Beyazıt, 34119, İstanbul, Türkiye
[11] Istanbul University, Science Faculty, Department of Astronomy and Space Sciences, Beyazıt, 34119, İstanbul, Türkiye
[12] Istanbul University Observatory Research and Application Center, Istanbul University, 34119, İstanbul, Türkiye
[13] Independent Researcher
[14] Department of Astronomy, University of Maryland, College Park, MD 20742, USA
[15] Center for Research and Exploration in Space Science & Technology II (CRESST II), NASA/GSFC, Greenbelt, MD 20771, USA
[16] IRAP, CNRS, 9 avenue du Colonel Roche, BP 44346, F-31028 Toulouse Cedex 4, France
[17] Université de Toulouse, CNES, UPS-OMP, F-31028 Toulouse, France
[18] The Catholic University of America, 620 Michigan Avenue, N.E. Washington, DC 20064, USA
[19] DTU Space, Technical University of Denmark, Elektrovej 327-328, DK-2800 Lyngby, Denmark
[20] International Space Science Institute, Hallerstrasse 6, 3012 Bern, Switzerland
Received 2024 April 29; revised 2024 May 11; accepted 2024 May 14; published 2024 June 6

Abstract

We present the discovery, with the Neutron Star Interior Composition Explorer (NICER), that SRGA J144459.2−604207 is a 447.9 Hz accreting millisecond X-ray pulsar (AMXP), which underwent a 4 week long outburst starting on 2024 February 15. The AMXP resides in a 5.22 hr binary, orbiting a low-mass companion donor with $M_d > 0.1\ M_\odot$. We report on the temporal and spectral properties from NICER observations during the early days of the outburst, from 2024 February 21 through 2024 February 23, during which NICER also detected a type I X-ray burst that exhibited a plateau lasting ∼6 s. The spectra of the persistent emission were well described by an absorbed thermal blackbody and power-law model, with blackbody temperature $kT \approx 0.9$ keV and power-law photon index $\Gamma \approx 1.9$. Time-resolved burst spectroscopy confirmed the thermonuclear nature of the burst, where an additional blackbody component reached a maximum temperature of nearly $kT \approx 3$ keV at the peak of the burst. We discuss the nature of the companion as well as the type I X-ray burst.

Unified Astronomy Thesaurus concepts: Neutron stars (1108); X-ray transient sources (1852); Millisecond pulsars (1062); X-ray bursts (1814); Low-mass x-ray binary stars (939)

1. Introduction

Accreting millisecond X-ray pulsars (AMXPs) are weakly magnetized ($B \sim 10^8$ G) neutron stars (NSs) with millisecond spin periods accreting from a low-mass companion donor, $M_d < 1\ M_\odot$ (see Di Salvo & Sanna 2022; Di Salvo et al. 2023, for recent reviews). AMXPs are believed to have formed from the sustained spin-up torque provided by accreted material from a donor undergoing Roche lobe overflow over Gyr timescales; this is known as the recycling scenario (Alpar et al. 1992). AMXPs represent the most extreme spin periods for collapsed stellar objects, and thus are excellent laboratories for testing the limits of accretion physics (Chakrabarty et al. 2003; Bhattacharyya & Chakrabarty 2017). By comparing the expected accretion luminosity produced by different orbital angular momentum sinks (e.g., magnetic braking and/or gravitational radiation) and the observed accretion luminosity during outbursts, AMXPs can be used to test mass transfer scenarios in these extreme systems (e.g., Marino et al. 2019a; Bult et al. 2021a; Ng et al. 2021). For example, in the latest outburst of SAX J1808.4−3658, the observed orbital evolution was proposed to be due to ejected material having a specific angular momentum equal to or greater than that of the companion (Applegate & Shaham 1994; Illiano et al. 2023). We can further refine the physics governing these systems through the discovery of additional AMXPs with all-sky multiwavelength monitoring of any transient outburst activity. These intermittent outbursts are likely the result of thermal instabilities in the accretion disk around the central NS (Lasota 2001).

The Mikhail Pavlinsky ART-XC telescope on the Spectrum-Roentgen-Gamma (SRG) observatory (Pavlinsky et al. 2021; Sunyaev et al. 2021) first reported the discovery of a bright

X-ray transient, SRGA J144459.2−604207, on 2024 February 21 (Mereminskiy et al. 2024). Additional data from the MAXI/Gas Slit Camera (GSC) X-ray sky monitor showed that the outburst actually began around February 15 (Mihara et al. 2024). This discovery was promptly followed up by an array of telescopes and instruments across many wavelengths. NICER discovered coherent X-ray pulsations at around 447.9 Hz and a type I X-ray burst in its initial observations (Ng et al. 2024). MeerKAT reported a nondetection at GHz radio wavelengths (Mariani et al. 2024), but the X-ray source localization provided by Chandra (Illiano et al. 2024) led to the detection of a GHz radio counterpart by ATCA (Russell et al. 2024). Optical follow-up observations did not detect an optical counterpart (Baglio et al. 2024; Cowie et al. 2024; Saikia et al. 2024; Sokolovsky et al. 2024). A candidate near-infrared counterpart was identified with the PRIME telescope (Guiffreda et al. 2024), but it is formally incompatible with the Chandra localization. Further observations by INTEGRAL (Sanchez-Fernandez et al. 2024a, 2024b) and NinjaSat (Takeda et al. 2024) detected type I X-ray bursts with recurrence timescales ranging from 1.7 to 2.9 hr, with the period increasing as the persistent emission flux decreased.

We present the NICER discovery of 447.9 Hz pulsations of the AMXP SRGA J144459.2−604207 and provide a preliminary timing solution for the orbital modulation of the pulse frequency. We also report on the discovery and characterization of the type I X-ray burst. It is the 27th known AMXP and the first AMXP outburst discovered by the ART-XC telescope. We note that after this manuscript was submitted, the ART-XC team reported on ART-XC observations of the source (Molkov et al. 2024). In Section 2, we present the NICER X-ray observations undertaken and the associated analysis procedures. We present the timing and spectroscopic results in Section 3 and discuss the results in Section 4.

2. Observations and Data Analysis

The Neutron Star Interior Composition Explorer (NICER) is an external payload on the International Space Station. It consists of 56 (52 operational) coaligned X-ray concentrator optics and silicon drift detectors in focal plane modules (FPMs). NICER provides fast-timing capabilities in the 0.2–12.0 keV energy range, and the onboard global positioning system receiver allows for 100 ns time-tagging accuracy (Gendreau et al. 2016; LaMarr et al. 2016; Prigozhin et al. 2016).

We report on public NICER observations conducted over 2024 February 21 through 2024 February 23 (MJD 60361–60363), with observation IDs (ObsIDs) 6204190101–6204190103. Additional NICER observations were conducted under the NICER Guest Observer program (PI: A. Papitto) and will be reported elsewhere. Our observations were reduced and processed with HEASOFT version 6.33 and the NICER Data Analysis Software (NICERDAS) version 12 (2024-02-09_V012) using calibration version `xti20240206`. We imposed the following filtering criteria for the observations: angular offset for the source of ANG_DIST $< 54''$; NICER being outside of the South Atlantic Anomaly; an Earth limb elevation angle of ELV $> 20°$; a bright Earth limb angle of BR_EARTH $> 30°$; an undershoot rate (per FPM; for dark current) of underonly_range = 0–500, and an overshoot rate (per FPM; for charged particle saturation) of overonly_range = 0–30. This resulted in good time intervals (GTIs) totaling 9.15 ks for scientific analysis.

We transformed the photon arrival times into the inertial frame of the solar system by performing the solar system barycenter corrections in the International Celestial Reference System reference frame with source coordinates R.A. = 221.°24558, decl. = − 60.°69869 (Illiano et al. 2024) obtained by Chandra, using `barycorr` in FTOOLS with the JPL DE421 solar system ephemeris (Folkner et al. 2009). We made use of `XSPEC` 12.14.0 (Arnaud 1996) for our spectral analysis. The generation of spectral products was enabled by the `nicerl3-spect` spectral product pipeline, which allowed us to group the spectra with the optimal binning; rebin the spectra so that each bin had a minimum of 25 counts (Kaastra & Bleeker 2016); generate background spectra using the `nibackgen3C50` model (Remillard et al. 2022); and generate the associated response matrices.

3. Results

We place the NICER observations in context of the overall outburst evolution from MAXI/GSC observations in Figures 1(a) and (b)—as reported in the figure zoom-in, the NICER observations analyzed were around the peak of the outburst.

3.1. X-Ray Pulsation Discovery and Timing

To search for coherent periodicity, we employed the Fourier-domain acceleration search (FDAS) method implemented in version 4.0 of the open-source pulsar search and analysis software `PRESTO` (Ransom 2011). The algorithm accounts for possible pulsation frequency modulations due to the binary Doppler effect with orbital period $P_{\rm orb}$ (Ransom et al. 2002). The FDAS were carried out on individual GTIs throughout the observation span of SRGA J144459.2−604207, with a minimum interval length of 100 s. We had 15 GTIs overall, with a median segment length of 613 s (spanning 183–911 s). We adopted this approach as the sensitivity of acceleration searches is optimized for segment lengths T such that $T \lesssim P_{\rm orb}/10$, as the pulsar acceleration is approximately constant and the spin frequency is expected to linearly evolve within the segment (Ransom et al. 2002). We searched over the 1–1000 Hz frequency range, and in two energy bands: 0.3–2.0 keV and 2.0–10.0 keV. We found significant candidates in several, but not all, GTIs within the 2.0–10.0 keV band. Specifically, we found 10 candidates around 447.9 Hz with single-trial significance over 2.5σ–5.5σ. Given the overall pulsation search parameter space, the pulsation signal corresponds to a trials-adjusted significance of 11.3σ (5.4×10^{10} trials) across all of the independent data segments, frequency bins, and Fourier bins searched.

With the secure detection of coherent X-ray pulsations, we proceeded to characterize the pulse. First, we derived a provisional circular orbit model by fitting an ellipse in the period-acceleration plane with the 10 significant candidates. Next, we performed an epoch folding search in approximately 1 ks intervals and modeled the residual frequency variations, resulting in revised orbital parameters from the initial estimate. We also maximized the profile variance (χ^2) from exploring a grid of values defined by the spin frequency (ν_0) and epoch of ascending node passage ($T_{\rm asc}$). Next, we optimized the pulse significance by calculating the H-statistic (de Jager et al. 1989) with two harmonics ($m = 2$)

$$H \equiv \max_{1 \leqslant m \leqslant 2} (Z_m^2 - 4m + 4), \quad (1)$$

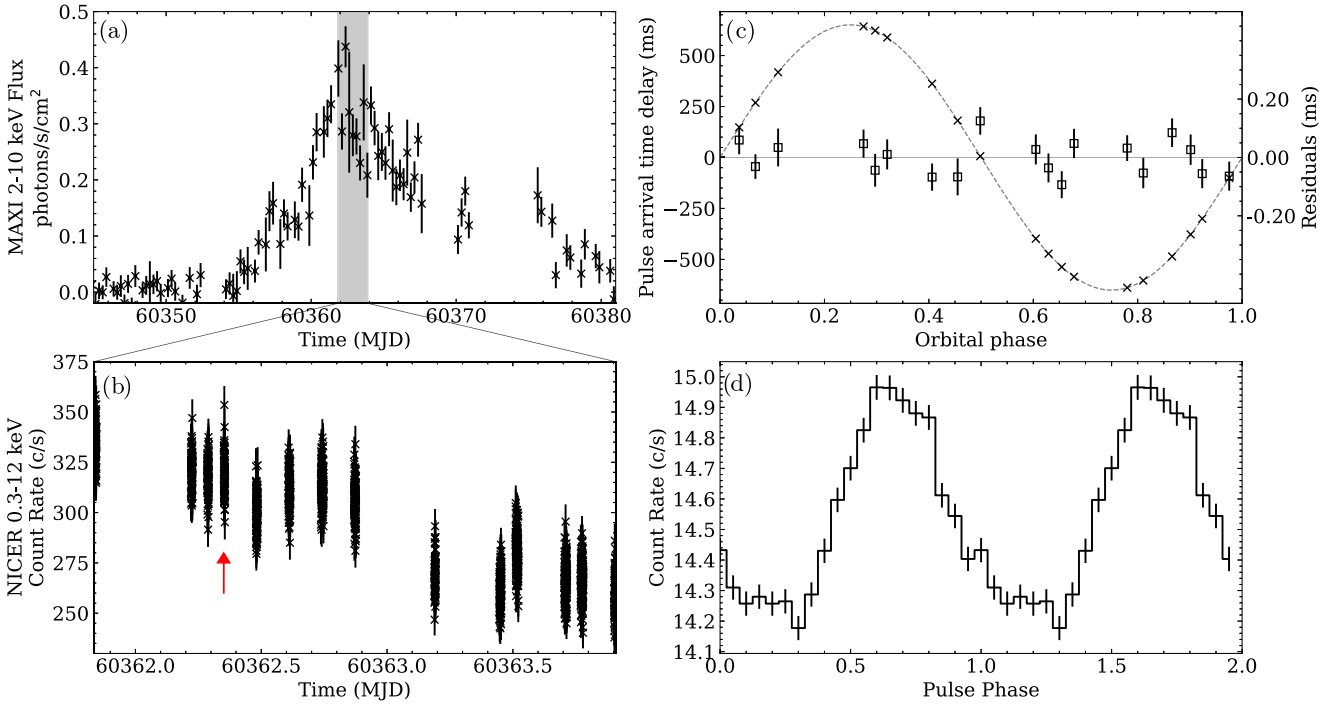

Figure 1. (a) SRGA J144459.2−604207 monitoring 2–10 keV light curve by MAXI/GSC (Mihara et al. 2024). The shaded gray region corresponds to the NICER observation interval. (b) NICER 0.3–12.0 keV light curve with 4 s bins. The burst emission was removed, but instead the midpoint of the burst interval (including the preburst) is shown with the red arrow. (c) The pulse arrival time delay as a function of the orbital phase, with the best-fit orbit shown with the dashed lines, and the pulse timing residuals shown in squares (with scale on the right y-axis). (d) Folded 1.0–10.0 keV pulse profile with the NICER observations. The profile also shows a significant second harmonic. There are 20 pulse phase bins and two cycles are plotted for clarity.

for

$$Z_m^2 = \frac{2}{N}\left[\left(\sum_{j=1}^{N}\cos 2m\pi\nu t_j\right)^2 + \left(\sum_{j=1}^{N}\sin 2m\pi\nu t_j\right)^2\right], \quad (2)$$

where t_j are the photon arrival times corrected for Doppler modulation described by the provisional orbit model ($j \in \{1,\ldots, N\}$ for N photons), over a grid of energy values (Buccheri et al. 1983). We found that the H-statistic was maximized for the energy range 1.03–11.97 keV. However, the H-statistic exhibited very little variance (maximum of $\Delta H = +2$) throughout the energy grid search. We adopted an energy range of 1.0–10.0 keV for the timing analysis as the background (see below) dominates below and above this energy range.

With this initial model, we generated 19 pulse times of arrival (TOAs) with the `photon_toa.py` tool in the `NICERsoft` data analysis package,[21] where each TOA had an integration time of 300 s (with minimum exposure time of 200 s). The TOAs were then correlated with a pulse template, using all of the data, comprising the sum of three Gaussians. Finally, we fit the pulse TOAs to the `ELL1` binary orbit model (Lange et al. 2001) available within PINT, an open-source pulsar timing `Python` package (Luo et al. 2021). The best-fit orbital ephemeris is given in Table 1, and the corresponding pulse arrival time delay (with respect to a constant spin frequency model) illustrating the best-fit orbit solution is shown in Figure 1(c). We note that the final orbital solution presented here is significantly different than the preliminary solutions previously reported both with the same NICER data (Ray et al. 2024) and from Insight-HXMT (Li et al. 2024). However, of these three solutions, the final solution we present here has a significantly larger maximum H-statistic value of 867.61, compared to 149.78 and 60.43, respectively. The final folded pulse profile is shown in Figure 1(d), where fitting a two-component sinusoid yielded fractional root-mean-squared amplitudes of $1.79\% \pm 0.04\%$ and $0.35\% \pm 0.04\%$, for the fundamental and second harmonic, respectively. The evolution of the pulse profile throughout the outburst and its energy dependence is outside the scope of this Letter, and will be reported elsewhere.

[21] https://github.com/paulray/NICERsoft/

Table 1
Timing Model for SRGA J144459.2−604207 from the 2024 February Outburst

Parameter	Value
R.A., α (J2000) (deg)	221.2455833
Decl., δ (J2000) (deg)	−60.6986944
Spin frequency, ν_0 (Hz)	447.87156100(11)
Spin epoch, t_0 (TDB)	MJD 60362.87145091
Binary period, $P_{\rm orb}$ (days)	0.2176354(5)
Projected semimajor axis, $a_x \sin i$ (lt-s)	0.650527(17)
Epoch of ascending node passage, $T_{\rm asc}$ (TDB)	MJD 60361.858933(3)
Eccentricity, e	$<4 \times 10^{-4}$ (3σ)
χ^2/dof	27.7/11

Note. The solar system barycenter corrections were performed using the source coordinates determined with Chandra High Resolution Camera observations of the source region (Illiano et al. 2024).

3.2. Type I X-Ray Burst

During the NICER observations, we detected a sharp, short-lived increase in the X-ray flux, which the light-curve evolution

Table 2
FRED and FRED + Plateau Best-fit Parameters to the Type I X-Ray Burst Light Curve

Parameter	FRED	FRED + Plateau
t_0 (s)	39.1 ± 0.3	40.7 ± 0.2
$t_{\rm pl}$ (s)	...	5.8 ± 0.7
τ_D (s)	10.0 ± 0.3	9.3 ± 0.4
τ_R (s)	7.7 ± 1.0	2.7 ± 0.5
A (s^{-1})	4300 ± 600	1900 ± 200
C (s^{-1})	324.3 ± 1.8	326.0 ± 1.7
χ^2/dof	343/318	295/317

Note. Reference time of MJD 60362.350531 (2) (TT units at NICER). The uncertainties are given to 1σ confidence level.

suggested was a type I X-ray burst. We first characterized the light curve ($f(t)$ as a function of time, t) by fitting with a hybrid fast-rise exponential-decay (FRED) model with a plateau (Barrière et al. 2015), described by

$$f(t) = \begin{cases} C & t \leqslant t_0 \\ A \exp\left(-\dfrac{\tau_R}{t-t_0} - \dfrac{t-t_0}{\tau_D}\right) + C & t_0 < t \leqslant t_{\rm pe} \\ A \exp\left(-2\sqrt{\dfrac{\tau_R}{\tau_D}}\right) + C & t_{\rm pe} < t \leqslant t_{\rm pe} + t_{\rm pl}, \\ A \exp\left(-\dfrac{\tau_R}{t-t_0-t_{\rm pl}} - \dfrac{t-t_0-t_{\rm pl}}{\tau_D}\right) + C & t > t_{\rm pe} + t_{\rm pl} \end{cases} \quad (3)$$

where C is the persistent flux level (s^{-1}), A is the burst amplitude (s^{-1}), t_0 is the burst onset time (in seconds), τ_R and τ_D are the rise and decay timescales (in seconds), respectively, $t_{\rm pe} = t_0 + \sqrt{\tau_R \tau_D}$ is the time at the peak (in seconds), and $t_{\rm pl}$ is the interval length of the plateau (in seconds). The corresponding best-fit parameters are given in Table 2. We show the results of the fit in Figure 2, where we also show residuals from fitting a simple FRED model (Figure 2(b)). While both models provide a reasonable description of the burst, the hybrid FRED and plateau model significantly improves the residuals around the burst peak. The simple FRED model can also be rejected with probability 1.4×10^{-11} compared to the hybrid FRED and plateau model according to the Akaike information criterion (Akaike 1974; Liddle 2007).

3.3. Spectroscopy

3.3.1. Persistent Emission

First, we defined several intervals for spectral extraction. The preburst interval was between MJD 60362.35006 to 60362.35047 (TT units at NICER; spanning about 35 s), 5 s before the burst onset. The burst interval was defined to be between MJD 60362.35047 to 60362.35146 (spanning about 85 s), 80 s after the burst onset. We also present fits to the individual ObsIDs, but for ObsID 6204190102 which contains the type I X-ray burst, we excised the preburst and burst intervals.

For the spectral fits, we adopted a line of sight hydrogen column density of $n_{\rm H} = 2.9 \times 10^{22}\,{\rm cm}^{-2}$. This value was determined from a joint fit of the spectra from the three ObsIDs (not shown; preburst and burst intervals removed), where we

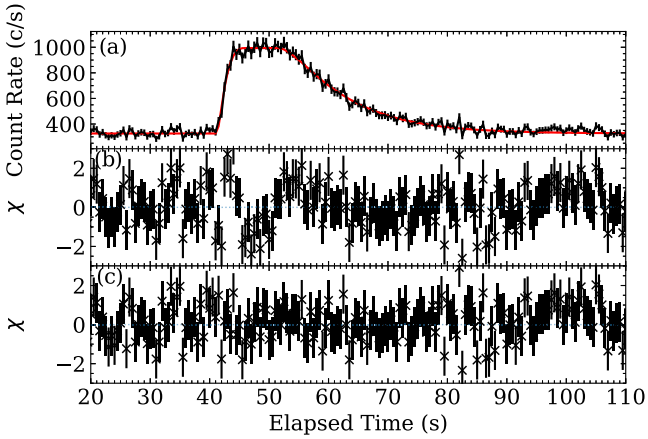

Figure 2. Phenomenological fit to the light curve of the type I X-ray burst in the NICER ObsID 6204190102 with a simple FRED model and a model with a FRED component and a plateau. (a) Light curve of the type I X-ray burst, with 0.5 s bins, with the FRED + plateau model shown in the solid red line; (b) residuals from fitting the burst light curve to a simple FRED model; (c) residuals from a FRED + plateau model. While the fit with the FRED model is formally acceptable (χ^2/dof = 1.08; 318 dof), the fit with the hybrid FRED and plateau model is significantly better at the 1.4×10^{-11} level, and the systematic residuals around the plateau are minimized. The elapsed time of 0 corresponds to MJD 60362.35007 (TT units at NICER).

employed an absorbed thermal blackbody and power-law model and untied all spectral parameters except for $n_{\rm H}$, and we found $n_{\rm H} = 2.90 \pm 0.03 \times 10^{22}\,{\rm cm}^{-2}$. All subsequent spectral fitting was restricted to 1.0–10.0 keV as the soft X-rays were absorbed below around 1.0 keV because of the high $n_{\rm H}$, and the background dominated above 10 keV. The `wilm` elemental abundance model was adopted for the spectral fits (Wilms et al. 2000). During the course of the three reported observations, the blackbody normalization remained constant within uncertainties, with an average value of ${\rm norm_{BB}} = 36.2^{+7.4}_{-5.8}\,(R_{\rm km}/D_{10})^2$, where $R_{\rm km}$ is the source region radius in kilometers, and D_{10} is the source distance in units of 10 kpc. The blackbody temperature marginally decreased from $kT = 0.99 \pm 0.08$ keV to $kT = 0.85^{+0.07}_{-0.06}$ keV, the photon index increased from $\Gamma = 1.81 \pm 0.03$ to $\Gamma = 1.90 \pm 0.02$, and the power-law normalization marginally decreased from ${\rm norm_{PL}} = 0.76 \pm 0.03$ photons s^{-1} cm^{-2} keV^{-1} to ${\rm norm_{PL}} = 0.69 \pm 0.03$ photons s^{-1} cm^{-2} keV^{-1}. The results are reported in Table 3. All uncertainties are reported at 90% confidence levels. The detailed spectroscopic evolution of the persistent emission during the entire outburst will be presented in a separate publication.

Next, we analyzed the preburst and burst intervals. The preburst spectrum was well described by an absorbed thermal blackbody and power-law model (`tbabs(bbodyrad+powerlaw)`), where $n_{\rm H} = 2.9 \times 10^{22}\,{\rm cm}^{-2}$ (fixed as per above), $kT = 0.99^{+0.20}_{-0.19}$ keV, ${\rm norm_{BB}} = 53^{+57}_{-25}(R_{\rm km}/D_{10})^2$, photon index $\Gamma = 1.92^{+0.14}_{-0.10}$, and ${\rm norm_{PL}} = 0.71 \pm 0.07$ photons s^{-1} cm^{-2} keV^{-1}.

3.3.2. Time-resolved Burst Spectroscopy

To further characterize the burst, we performed time-resolved spectroscopy starting from 5 s before burst onset, to 40 s after burst onset. We generated dynamically binned spectra, ensuring that each spectrum contained at least 2000 photons, and used `nicerl3-spect` to generate the associated responses. We used the `nibackgen3C50` background spectrum corresponding to ObsID 6204190102, as the background is not expected to vary significantly over the burst. We

Table 3
Spectroscopic Results for Individual ObsIDs with an Absorbed Thermal Blackbody and Power Law (`tbabs(bbodyrad+powerlaw)` in `XSPEC`)

	ObsID		
Parameter	6204190101	6204190102	6204190103
kT	$0.99^{+0.08}_{-0.08}$	$0.95^{+0.07}_{-0.06}$	$0.85^{+0.07}_{-0.06}$
$\mathrm{norm_{BB}}$	38^{+13}_{-10}	35^{+11}_{-9}	35^{+15}_{-11}
Γ	1.81 ± 0.03	1.82 ± 0.02	1.90 ± 0.02
$\mathrm{norm_{PL}}$	0.76 ± 0.03	0.73 ± 0.03	0.69 ± 0.03
$F_{1-10\ \mathrm{keV}}$	$2.648^{+0.014}_{-0.033}$	$2.448^{+0.008}_{-0.013}$	$2.009^{+0.006}_{-0.014}$
χ^2/dof	98.2/123	141.0/139	148.7/137

Note. The uncertainties are given to 90% confidence level. The parameter $\mathrm{norm_{BB}}$ is scaled by $(R_{\mathrm{km}}/D_{10})^2$ and $\mathrm{norm_{PL}}$ has units of photons $\mathrm{keV^{-1}\ cm^{-2}\ s^{-1}}$. The absorbed 1.0–10.0 keV flux, $F_{1-10\ \mathrm{keV}}$ is expressed in units of 10^{-9} erg $\mathrm{s^{-1}\ cm^{-2}}$.

also regrouped the spectra such that each spectral bin had a minimum of 25 counts. Given that the background dominated above 6.5 keV, the spectral fits were restricted to 1.0–6.5 keV. We fixed the parameters of the preburst model, and added a second thermal blackbody model to account for the burst evolution (the full model is `tbabs(bbodyrad+powerlaw +bbodyrad)`), which is shown in Figure 3. The burst decay was well described by a cooling thermal blackbody component, which supports the thermonuclear origin for the X-ray burst. Motivated by bursters that have exhibited excess emission above the burst, we tried to fit the spectra by including a scaling factor to the underlying preburst emission (Worpel et al. 2013, 2015; Güver et al. 2022a, 2022b), but it did not statistically improve the spectral fits. This is similar to what has been seen in sources with relatively higher hydrogen column density values of $n_{\mathrm{H}} > 10^{22}\ \mathrm{cm^{-2}}$ (Bult et al. 2021b; Güver et al. 2021; Bostancıet al. 2023). The bolometric unabsorbed flux shown in Figure 3(a) was derived using the convolutional `cflux` model, and we extrapolated the model out to 0.1–100 keV by using the `energies` command in `XSPEC`.

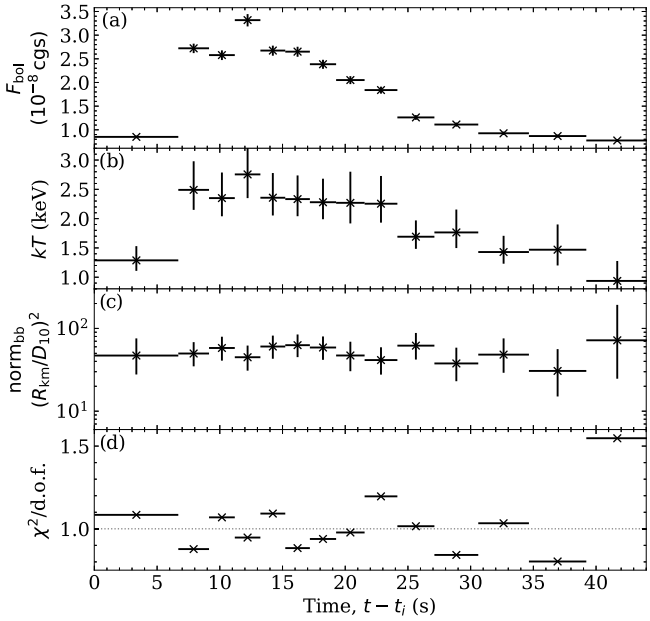

Figure 3. Evolution of the second blackbody component during the type I X-ray burst from time-resolved spectroscopy. (a) bolometric (0.1–100.0 keV) unabsorbed flux in units of 10^{-8} erg $\mathrm{s^{-1}\ cm^{-2}}$; (b) blackbody temperature, kT (keV); (c) blackbody normalization, $\mathrm{norm_{bb}}$ scaled by $(R_{\mathrm{km}}/D_{10})^2$; (d) reduced χ^2 for the fit. The cooling blackbody, the key signature of the thermonuclear nature of the burst, is evident. The offset, t_i, corresponds to MJD 60362.35047 (TT units at NICER).

4. Discussion

We have presented the NICER discovery of 447.9 Hz pulsations of the accreting millisecond X-ray pulsar SRGA J144459.2−604207, which resides in a 5.22 hr binary. We reported on initial NICER observations of the source around the peak of the outburst, from 2024 February 21 to 23. The observations also revealed a type I X-ray burst, and time-resolved burst spectroscopy confirmed the thermonuclear nature of the burst.

The determination of the binary orbital parameters of the SRGA J144459.2−604207 system allows us to constrain the properties of the companion/mass donor. We can employ the binary mass function,

$$f_m = \frac{(M_d \sin i)^3}{(M_{\mathrm{ns}} + M_d)^2} = \frac{4\pi^2 (a_x \sin i)^3}{G P_{\mathrm{orb}}^2}, \quad (4)$$

where M_d and M_{ns} are the donor and NS masses, respectively, and G is the gravitational constant. Assuming $M_{\mathrm{ns}} = 1.4\ M_\odot$, we plot the donor mass–radius curve from Equation (4) assuming a Roche-lobe-filling donor, which is shown in Figure 4. We also plot mass–radius curves for several companion types, including white dwarfs (WDs; Deloye & Bildsten 2003) and zero-age main-sequence stars (Tout et al. 1996). We found that for all plausible cold (core temperature, $T_c < 10^6$ K) and hot ($T_c > 10^6$ K) WDs, the WDs are too small to fill their Roche lobes to be viable companions for SRGA J144459.2−604207.

On the other hand, main-sequence (H-rich) companions are much more likely. For semidetached binaries such as the Roche-lobe-filling donor and AMXP here, the period−density relation $\bar{\rho} \simeq 107 (P_{\mathrm{orb}}/1\ \mathrm{hr})^{-2}\ \mathrm{g\ cm^{-3}}$ (Knigge et al. 2011) estimates a stellar mean density, $\bar{\rho}$ of around $\bar{\rho} \approx 4.0\ \mathrm{g\ cm^{-3}}$, which suggests an early M-type main-sequence donor (Drilling & Landolt 2000). While the mass–radius curve presented here is for solar metallicity ($Z = Z_\odot = 0.02$), for donor masses below $1\ M_\odot$, the mass–radius curves are weakly sensitive to the metallicity (Tout et al. 1996). The mass–radius curves for SRGA J144459.2−604207 and the main-sequence companion intersect at around $0.65\ M_\odot$, which corresponds to an a priori probability over binary inclination of $P(i \leqslant i_{0.65\ \mathrm{M}_\odot}) \approx 11\%$ assuming an isotropic population of binary inclinations. Consequently, most of the probability space, after considering binary inclination, lies above the main sequence in the mass–radius plane, indicating stars larger than a main-sequence star at the same mass. The main-sequence companion could have a bloated H atmosphere due to the X-ray irradiation by the NS, thus allowing for less massive (i.e., more probable) donors. Additionally, since we do not have full orbital coverage with this current data set, and given the noncontiguous nature of NICER observations, we cannot provide further inclination constraints through searches for dips or eclipses.

It is also much more plausible that the companion star is very old (∼Gyr) given the recycled nature of the system (e.g., Altamirano et al. 2008; Sanna et al. 2018), and the stellar isochrones for these old companions suggest a lower (more

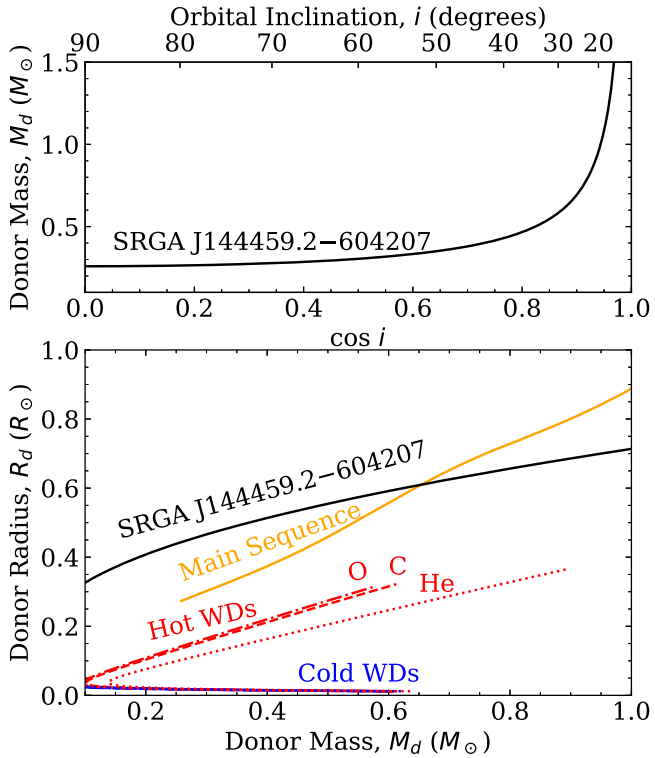

Figure 4. Top: donor mass (M_d, $M_\odot$) as a function of the binary inclination, i, for $M_{\rm ns} = 1.4\ M_\odot$; $1 - \cos i$ is the a priori cumulative distribution function of observed binary inclinations. Bottom: donor radius (R_d, $R_\odot$) as a function of the donor mass for SRGA J144459.2−604207 (black solid line), zero-age main-sequence stars (orange solid line; Tout et al. 1996), and hot (red) and cold (blue) WDs of varying compositions (Deloye & Bildsten 2003). The most viable donor for SRGA J144459.2−604207 is a main-sequence star (which may be slightly bloated).

plausible) mass (Girardi et al. 2000). The spin and orbital properties of SRGA J144459.2−604207, along with the derived companion properties, fit well within the population of known AMXPs with main-sequence companions (e.g., Papitto et al. 2007; Altamirano et al. 2011; Papitto et al. 2011; Riggio et al. 2011; Papitto et al. 2013; Patruno & Watts 2021). While we used $M_{\rm ns} = 1.4\ M_\odot$, we note that the mass–radius relation for SRGA J144459.2−604207 depends weakly on the NS mass. However, recycled pulsars which experienced low levels of sustained accretion over long timescales (∼Gyr) should have higher masses (Romani 1990; Romani et al. 2022).

NICER has detected a type I X-ray burst within the observation interval covered in this Letter. The burst light-curve profile was best fit with a phenomenological hybrid fast-rise exponential decay and plateau model (see Table 2). The burst duration of <100 s suggests low accretion rates of mixed H/He material (Fujimoto et al. 1987; in't Zand et al. 2005). Time-resolved burst spectroscopy as shown in Figure 3 revealed a constant blackbody normalization during the burst, suggesting that a photospheric radius expansion (PRE) event did not take place. However, we can derive an upper limit on the source distance assuming that the burst peak was at Eddington luminosity. The peak bolometric (0.1–100.0 keV) unabsorbed flux was around 2.8×10^{-8} erg s^{-1} cm^{-2}, and given the empirical critical luminosity of 3.8×10^{38} erg s^{-1} at the peak of type I X-ray bursts during PRE events, this implies an upper limit on the source distance of $d < 10.6$ kpc (Kuulkers et al. 2003).

Subsequent NICER observations, as well as those by other instruments such as Swift/X-Ray Telescope (Mariani et al. 2024), INTEGRAL (Sanchez-Fernandez et al. 2024a, 2024b), and NinjaSat (Takeda et al. 2024) have detected more type I X-ray bursts from SRGA J144459.2−604207. In fact, INTEGRAL reported the "quasiperiodic" nature of the type I X-ray burst trains, with a burst recurrence rate that is a function of the outburst flux (Sanchez-Fernandez et al. 2024b). Earlier INTEGRAL observations noted a recurrence timescale of about 1.7 hr over 60 ks, implying a remarkably stable accretion rate (Sanchez-Fernandez et al. 2024a). There are three other known sources that have exhibited clocked bursting behavior. The canonical Clocked Burster (GS 1826−238) had regular burst recurrence timescales between 3.6 and 5.7 hr since its outburst onset in 1988 (Ubertini et al. 1999; Chenevez et al. 2016), though its bursting activity has dramatically reduced upon its transition into the spectrally softer "banana" state in 2016 (Chenevez et al. 2016; Yun et al. 2023). The other known clocked burster, 1RXS J180408.9−342058, was found to display clocked bursting behavior in its intermediate spectral state, with a recurrence timescales of around 0.9 hr (Marino et al. 2019b). The 11 Hz burster IGR J17480−2446 also exhibited clocklike bursting activity (Chakraborty et al. 2011). Such behavior is thought to be related to the near-solar composition of the accreted material (Galloway et al. 2004; Heger et al. 2007; Lampe et al. 2016; Meisel 2018). We note that this is the second clocked burster for which we know the spin period and orbital properties, the other being IGR J17480−2446 (Strohmayer et al. 2010; Motta et al. 2011). A detailed study of the broadband timing and spectral properties of the type I X-ray bursts from the outburst of SRGA J144459.2−604207 is outside of the scope of this Letter and will be reported in a future publication.

Assuming an averaged unabsorbed bolometric (0.1–100.0 keV) flux across the three observations of $F = 7 \times 10^{-9}$ erg s^{-1} cm^{-2}, then for $d < 10.6$ kpc, the source luminosity is estimated to be $L < 9.5 \times 10^{37}$ erg s^{-1}. If we assume spin equilibrium, then the dipolar NS magnetic field is approximately

$$B = 4.2\zeta^{-\frac{7}{6}}\left(\frac{P}{10\ \mathrm{ms}}\right)^{\frac{7}{6}}\left(\frac{M_{\rm ns}}{1.4\ M_\odot}\right)^{\frac{1}{3}}\left(\frac{\dot{M}}{10^{-10}\ M_\odot/\mathrm{yr}}\right)^{\frac{1}{2}} 10^8\ G, \quad (5)$$

where ζ is the order-unity ratio of the magnetospheric and Alfvén radii (Ghosh & Lamb 1979), $P = 1/\nu$ is the pulsar spin period, and $\dot{M}$ is the mass transfer rate from the donor onto the NS. For an NS with radius $R = 10$ km and $M_{\rm ns} = 1.4\ M_\odot$, we find for $d < 10.6$ kpc that $\dot{M} < 8.11 \times 10^{-9}(d/10.6\mathrm{kpc})^2\ M_\odot/\mathrm{yr}$. Thus for $d < 10.6$ kpc, $B < (6.6 - 96.6) \times 10^8$ G, which is within expectations (albeit a large range) from the distribution of estimated magnetic field strengths of AMXPs (Mukherjee et al. 2015).

A more accurate determination of the magnetic field strength will come from observing more outbursts from SRGA J144459.2−604207 to measure a long-term spin frequency derivative, $\dot{\nu}$. In fact, MAXI/GSC found signs of past weak activity in 2022 January and 2023 December (Negoro et al. 2024), and INTEGRAL reported significant hard X-ray activity in 2023 December (Sguera & Sidoli 2024), but there were no dense monitoring observations available for those periods. Further

X-ray monitoring observations will be crucial in detecting the rising outbursts of SRGA J144459.2−604207 to further constrain the source properties, such as the evolution of the type I X-ray burst morphology. Further all-sky high-cadence multiwavelength surveys will be instrumental in discovering more AMXPs to understand the population and diversity of phenomena they exhibit.

Acknowledgments

This research has made use of data and/or software provided by the High Energy Astrophysics Science Archive Research Center (HEASARC), which is a service of the Astrophysics Science Division at NASA/GSFC and the High Energy Astrophysics Division of the Smithsonian Astrophysical Observatory. This research has made use of MAXI data provided by RIKEN, JAXA and the MAXI team. NICER work at NRL is supported by NASA. M.N. was supported in part by NASA through the NICER Guest Observer Program. A.P. and G.I. acknowledge financial support from the National Institute for Astrophysics (INAF) Research Grant "Uncovering the optical beat of the fastest magnetised neutron stars (FANS)" and the Italian Ministry of University and Research (MUR) under PRIN 2020 grant No. 2020BRP57Z "Gravitational and Electromagnetic-wave Sources in the Universe with current and next-generation detectors (GEMS)." T.G. and T.B. are supported by the Scientific Research Projects Coordination Unit of Istanbul University (ADEP Project No: FBA-2023-39409). J.H. acknowledges support from NASA under award No. 80GSFC21M0002.

Facilities: NICER, MAXI

Software: Astropy (Astropy Collaboration et al. 2013, 2018), PRESTO (Ransom et al. 2002), NumPy and SciPy (Virtanen et al. 2020), Matplotlib (Hunter 2007), IPython (Perez & Granger 2007), tqdm (da Costa-Luis et al. 2022), HEASoft 6.33[22] (NASA High Energy Astrophysics Science Archive Research Center (HEASARC), 2014).

ORCID iDs

Mason Ng https://orcid.org/0000-0002-0940-6563
Paul S. Ray https://orcid.org/0000-0002-5297-5278
Andrea Sanna https://orcid.org/0000-0002-0118-2649
Tod E. Strohmayer https://orcid.org/0000-0001-7681-5845
Alessandro Papitto https://orcid.org/0000-0001-6289-7413
Giulia Illiano https://orcid.org/0000-0003-4795-7072
Arianna C. Albayati https://orcid.org/0000-0001-5472-0554
Diego Altamirano https://orcid.org/0000-0002-3422-0074
Tuğba Boztepe https://orcid.org/0000-0002-4729-1592
Tolga Güver https://orcid.org/0000-0002-3531-9842
Deepto Chakrabarty https://orcid.org/0000-0001-8804-8946
Zaven Arzoumanian https://orcid.org/0009-0008-6187-8753
D. J. K. Buisson https://orcid.org/0000-0002-5341-6929
Elizabeth C. Ferrara https://orcid.org/0000-0001-7828-7708
Keith C. Gendreau https://orcid.org/0000-0001-7115-2819
Sebastien Guillot https://orcid.org/0000-0002-6449-106X
Jeremy Hare https://orcid.org/0000-0002-8548-482X
Gaurava K. Jaisawal https://orcid.org/0000-0002-6789-2723
Christian Malacaria https://orcid.org/0000-0002-0380-0041
Michael T. Wolff https://orcid.org/0000-0002-4013-5650

[22] http://heasarc.gsfc.nasa.gov/ftools

References

Akaike, H. 1974, ITAC, 19, 716
Alpar, M. A., Hasinger, G., Shaham, J., & Yancopoulos, S. 1992, A&A, 257, 627
Altamirano, D., Casella, P., Patruno, A., Wijnands, R., & van der Klis, M. 2008, ApJL, 674, L45
Altamirano, D., Cavecchi, Y., Patruno, A., et al. 2011, ApJL, 727, L18
Applegate, J. H., & Shaham, J. 1994, ApJ, 436, 312
Arnaud, K. A. 1996, in ASP Conf. Ser. 101, Astronomical Data Analysis Software and Systems V, ed. G. H. Jacoby & J. Barnes (San Francisco, CA: ASP), 17
Astropy Collaboration, Price-Whelan, A. M., Sipőcz, B. M., et al. 2018, AJ, 156, 123
Astropy Collaboration, Robitaille, T. P., Tollerud, E. J., et al. 2013, A&A, 558, A33
Baglio, M. C., Russell, D. M., Saikia, P., et al. 2024, ATel, 16487, 1
Barrière, N. M., Krivonos, R., Tomsick, J. A., et al. 2015, ApJ, 799, 123
Bhattacharyya, S., & Chakrabarty, D. 2017, ApJ, 835, 4
Bostancı, Z. F., Boztepe, T., Güver, T., et al. 2023, ApJ, 958, 55
Buccheri, R., Bennett, K., Bignami, G. F., et al. 1983, A&A, 128, 245
Bult, P., Altamirano, D., Arzoumanian, Z., et al. 2021b, ApJ, 907, 79
Bult, P., Strohmayer, T. E., Malacaria, C., Ng, M., & Wadiasingh, Z. 2021a, ApJ, 912, 120
Chakrabarty, D., Morgan, E. H., Muno, M. P., et al. 2003, Natur, 424, 42
Chakraborty, M., Bhattacharyya, S., & Mukherjee, A. 2011, MNRAS, 418, 490
Chenevez, J., Galloway, D. K., in 't Zand, J. J. M., et al. 2016, ApJ, 818, 135
Cowie, F. J., Gillanders, J. H., Rhodes, L., et al. 2024, ATel, 16477, 1
da Costa-Luis, C., Larroque, S. K., Altendorf, K., et al. 2022, tqdm: A fast, Extensible Progress Bar for Python and CLI, v4.64.0, Zenodo, doi:10.5281/zenodo.6412640
de Jager, O. C., Raubenheimer, B. C., & Swanepoel, J. W. H. 1989, A&A, 221, 180
Deloye, C. J., & Bildsten, L. 2003, ApJ, 598, 1217
Di Salvo, T., Papitto, A., Marino, A., Iaria, R., & Burderi, L. 2023, in Handbook of X-ray and Gamma-ray Astrophysics, ed. C. Bambi & A. Santangelo (Singapore: Springer)
Di Salvo, T., & Sanna, A. 2022, in Astrophysics and Space Science Library, ed. S. Bhattacharyya, A. Papitto, & D. Bhattacharya, Vol. 465 (Cham: Springer), 87
Drilling, J. S., & Landolt, A. U. 2000, in Allen's Astrophysical Quantities, ed. A. N. Cox (New York: Springer), 381
Folkner, W. M., Williams, J. G., & Boggs, D. H. 2009, IPNPR, 42-178, 1
Fujimoto, M. Y., Sztajno, M., Lewin, W. H. G., & van Paradijs, J. 1987, ApJ, 319, 902
Galloway, D. K., Cumming, A., Kuulkers, E., et al. 2004, ApJ, 601, 466
Gendreau, K. C., Arzoumanian, Z., Adkins, P. W., et al. 2016, Proc. SPIE, 601, 99051H
Ghosh, P., & Lamb, F. K. 1979, ApJ, 232, 259
Girardi, L., Bressan, A., Bertelli, G., & Chiosi, C. 2000, A&AS, 141, 371
Guiffreda, O., De, K., Durbak, J., et al. 2024, Atel, 16499, 1
Güver, T., Bostancı, Z. F., Boztepe, T., et al. 2022b, ApJ, 935, 154
Güver, T., Boztepe, T., Ballantyne, D. R., et al. 2022a, MNRAS, 510, 1577
Güver, T., Boztepe, T., Göğüş, E., et al. 2021, ApJ, 910, 37
Heger, A., Cumming, A., Galloway, D. K., & Woosley, S. E. 2007, ApJL, 671, L141
Hunter, J. D. 2007, CSE, 9, 90
Illiano, G., Papitto, A., Sanna, A., et al. 2023, ApJL, 942, L40
Illiano, G., Zelati, F. C., Marino, A., et al. 2024, ATel, 16510, 1
in't Zand, J. J. M., Cornelisse, R., & Méndez, M. 2005, A&A, 440, 287
Kaastra, J. S., & Bleeker, J. A. M. 2016, A&A, 587, A151
Knigge, C., Baraffe, I., & Patterson, J. 2011, ApJS, 194, 28
Kuulkers, E., den Hartog, P. R., in't Zand, J. J. M., et al. 2003, A&A, 399, 663
LaMarr, B., Prigozhin, G., Remillard, R., et al. 2016, Proc. SPIE, 9905, 99054W
Lampe, N., Heger, A., & Galloway, D. K. 2016, ApJ, 819, 46
Lange, C., Camilo, F., Wex, N., et al. 2001, MNRAS, 326, 274
Lasota, J.-P. 2001, NewAR, 45, 449
Li, Z., Kuiper, L., Falanga, M., et al. 2024, ATel, 16548, 1
Liddle, A. R. 2007, MNRAS, 377, L74
Luo, J., Ransom, S., Demorest, P., et al. 2021, ApJ, 911, 45
Mariani, I., Motta, S., Baglio, M. C., et al. 2024, ATel, 16475, 1
Marino, A., Del Santo, M., Cocchi, M., et al. 2019b, MNRAS, 490, 2300

Marino, A., Di Salvo, T., Burderi, L., et al. 2019a, A&A, 627, A125
Meisel, Z. 2018, ApJ, 860, 147
Mereminskiy, I. A., Semena, A. N., Molkov, S. V., et al. 2024, ATel, 16464, 1
Mihara, T., Negoro, H., Nakajima, M., et al. 2024, ATel, 16469, 1
Molkov, S. V., Lutovinov, A. A., Tsygankov, S. S., et al. 2024, arXiv:2404.19709
Motta, S., D'Aì, A., Papitto, A., et al. 2011, MNRAS, 414, 1508
Mukherjee, D., Bult, P., van der Klis, M., & Bhattacharya, D. 2015, MNRAS, 452, 3994
NASA High Energy Astrophysics Science Archive Research Center (HEASARC) 2014, HEAsoft: Unified Release of FTOOLS and XANADU, Astrophysics Source Code Library, ascl:1408.004
Negoro, H., Mihara, T., Serino, M., et al. 2024, ATel, 16483, 1
Ng, M., Ray, P. S., Bult, P., et al. 2021, ApJL, 908, L15
Ng, M., Sanna, A., Strohmayer, T. E., et al. 2024, ATel, 16474, 1
Papitto, A., Bozzo, E., Ferrigno, C., et al. 2011, A&A, 535, L4
Papitto, A., di Salvo, T., Burderi, L., et al. 2007, MNRAS, 375, 971
Papitto, A., Ferrigno, C., Bozzo, E., et al. 2013, Natur, 501, 517
Patruno, A., & Watts, A. L. 2021, in Astrophysics and Space Science Library, Timing Neutron Stars: Pulsations, Oscillations and Explosions, ed. T. M. Belloni, M. Méndez, & C. Zhang, Vol. 461 (Berlin: Springer), 143
Pavlinsky, M., Tkachenko, A., Levin, V., et al. 2021, A&A, 650, A42
Perez, F., & Granger, B. E. 2007, CSE, 9, 21
Prigozhin, G., Gendreau, K., Doty, J. P., et al. 2016, Proc. SPIE, 9905, 99051I
Ransom, S. 2011, Astrophysics Source Code Library, ascl:1107.017
Ransom, S. M., Eikenberry, S. S., & Middleditch, J. 2002, AJ, 124, 1788
Ray, P. S., Strohmayer, T. E., Sanna, A., et al. 2024, ATel, 16480, 1
Remillard, R. A., Loewenstein, M., Steiner, J. F., et al. 2022, AJ, 163, 130
Riggio, A., Papitto, A., Burderi, L., et al. 2011, A&A, 526, A95
Romani, R. W. 1990, Natur, 347, 741
Romani, R. W., Kandel, D., Filippenko, A. V., Brink, T. G., & Zheng, W. 2022, ApJL, 934, L17
Russell, T. D., Carotenuto, F., & Eijnden, J. V. D. 2024, ATel, 16511, 1
Saikia, P., Russell, D. M., Baglio, M. C., et al. 2024, ATel, 16489, 1
Sanchez-Fernandez, C., Kuulkers, E., Ferrigno, C., & Chenevez, J. 2024a, ATel, 16485, 1
Sanchez-Fernandez, C., Kuulkers, E., Ferrigno, C., Chenevez, J., & Del Santo, M. 2024b, ATel, 16507, 1
Sanna, A., Ferrigno, C., Ray, P. S., et al. 2018, A&A, 617, L8
Sguera, V., & Sidoli, L. 2024, ATel, 16493, 1
Sokolovsky, K., Korotkiy, S., & Zalles, R. 2024, ATel, 16476, 1
Strohmayer, T. E., Markwardt, C. B., Pereira, D., & Smith, E. A. 2010, ATel, 2946, 1
Sunyaev, R., Arefiev, V., Babyshkin, V., et al. 2021, A&A, 656, A132
Takeda, T., Ota, N., Watanabe, S., et al. 2024, ATel, 16495, 1
Tout, C. A., Pols, O. R., Eggleton, P. P., & Han, Z. 1996, MNRAS, 281, 257
Ubertini, P., Bazzano, A., Cocchi, M., et al. 1999, ApJL, 514, L27
Virtanen, P., Gommers, R., Oliphant, T. E., et al. 2020, NatMe, 17, 261
Wilms, J., Allen, A., & McCray, R. 2000, ApJ, 542, 914
Worpel, H., Galloway, D. K., & Price, D. J. 2013, ApJ, 772, 94
Worpel, H., Galloway, D. K., & Price, D. J. 2015, ApJ, 801, 60
Yun, S. B., Grefenstette, B. W., Ludlam, R. M., et al. 2023, ApJ, 947, 81